Check for updates

View Article Online
View Journal

Chemical Science

Accepted Manuscript

This article can be cited before page numbers have been issued, to do this please use: E. P. Craddock, J. L. Shelton, M. T. Ruggiero and K. E. Knowles, *Chem. Sci.*, 2025, DOI: 10.1039/D5SC01909E.

This is an Accepted Manuscript, which has been through the Royal Society of Chemistry peer review process and has been accepted for publication.

Accepted Manuscripts are published online shortly after acceptance, before technical editing, formatting and proof reading. Using this free service, authors can make their results available to the community, in citable form, before we publish the edited article. We will replace this Accepted Manuscript with the edited and formatted Advance Article as soon as it is available.

You can find more information about Accepted Manuscripts in the Information for Authors.

Please note that technical editing may introduce minor changes to the text and/or graphics, which may alter content. The journal's standard Terms & Conditions and the Ethical guidelines still apply. In no event shall the Royal Society of Chemistry be held responsible for any errors or omissions in this Accepted Manuscript or any consequences arising from the use of any information it contains.

ROYAL SOCIETY OF CHEMISTRY

rsc.li/chemical-science

View Article Online
DOI: 10.1039/D5SC01909E

Local Coordination Geometry within Cobalt Spinel Oxides Mediates Photoinduced Polaron Formation

Erica P. Craddock,[†] Jacob L. Shelton,[†,‡] Michael T. Ruggiero,[†] Kathryn E. Knowles[†*]

[†]*Department of Chemistry, University of Rochester, Rochester NY 14627, USA*

*corresponding author e-mail: kknowles@ur.rochester.edu

Open Access Article. Published on 12 May 2025. Downloaded on 5/16/2025 10:21:16 PM.
This article is licensed under a Creative Commons Attribution 3.0 Unported Licence.

ABSTRACT – Understanding the photophysics of transition metal oxides is crucial for these materials to realize their considerable potential in applications such as photocatalysis and optoelectronics. Recent studies suggest that formation of localized excited states consisting of polarons (quasi-particles comprising a charge carrier strongly coupled to a proximal lattice distortion) plays a crucial role in the photophysics of these materials. Cobalt-containing spinel oxides (Co_3O_4 and $ZnCo_2O_4$) offer a unique opportunity to investigate the influence of local geometry, and cation inversion on photoinduced polaron formation. Here, we use Hubbard-corrected density functional theory (DFT+U) paired with resonance Raman and temperature-dependent optical spectroscopies to demonstrate that low-energy transitions observed in Co_3O_4 are associated with *d-d* transitions involving cobalt ions occupying tetrahedral sites within the spinel lattice. These low-energy optical transitions exhibit strong coupling to phonon modes associated with tetrahedral sites. Replacing most tetrahedral cobalt ions with zinc produces the slightly inverted ternary spinel material, $ZnCo_2O_4$, in which we observe a phonon-coupled optical transition that occurs at the same energy as observed in Co_3O_4. We propose that these phonon-coupled optical transitions enable direct access to a polaronic state upon photoexcitation; however, the intensity of this optical transition depends on temperature in Co_3O_4, whereas no significant temperature dependence is observed in $ZnCo_2O_4$. We therefore hypothesize that in Co_3O_4 the mechanism of polaron formation is coupling of the optical transition to dynamic, thermally-gated lattice distortions, whereas, in $ZnCo_2O_4$, the transition couples to static lattice defects that arise from the presence of a small population of tetrahedrally-coordinated cobalt ions.

[‡]current address: National Renewable Energy Laboratory, Chemistry and Nanoscience Center, Golden, CO, 80401, USA

Chemical Science Accepted Manuscript

View Article Online
DOI: 10.1039/D5SC01909E

Open Access Article. Published on 12 May 2025. Downloaded on 5/16/2025 10:21:16 PM.
This article is licensed under a Creative Commons Attribution 3.0 Unported Licence.

INTRODUCTION

Transition metal oxides have promising characteristics for solar energy conversion technologies because of their visible band gap energies, stability, abundance, cost-effectiveness and low toxicity.[1,2] However, these materials contain weakly dispersive bands originating from the metal 3*d* orbitals that lead to low charge-carrier mobility,[3,4] rapid charge recombination,[5,6] and formation of localized, "self-trapped" states near the band-edges.[7] These states, which comprise one or more localized charge carriers coupled to proximal lattice distortions arising from one or more phonons, are known as polarons.[7,8] Small polarons, first described by Holstein,[9,10] are described by a short-range carrier-phonon interaction ($radius_{polaron}$ ~ lattice parameter) and carrier mobility that increases with increased temperature.[11] Conversely, large polarons have long-range carrier-phonon interactions ($radius_{polaron}$ >> lattice parameter) with carrier mobility that decreases with increased temperature.[12,13] Many transition metal oxides are reported to host small polarons,[7,14–19] and in many cases the performance of these materials for electrocatalytic, photoelectrocatalytic, and/or optoelectronic applications is impacted by small polaron formation.[20–25]

Although conductivity studies have contributed to a thorough understanding of polaron transport mechanisms in transition metal oxides,[11,15,17,26,27] there is still a limited understanding of the mechanisms by which polarons form in photoexcited states. In hematite (α-Fe_2O_3), for example, one proposed mechanism involves indirect population of polaron states via relaxation from an initially excited, higher-energy non-polaronic state.[20,28] Our group recently identified an additional mechanism involving the direct population of polaronic excited states at room temperature upon band-edge excitation in α-Fe_2O_3.[29,30] Figure 1 depicts the difference between indirect and direct population of polaronic states via photoexcitation. Importantly, optical population of polaronic states in α-Fe_2O_3 is proposed to occur even in a pristine, defect-free lattice: the optical transitions couple to intrinsic, thermally-activated phonon distortions within the crystal.[29,30] There is also evidence of polaron formation arising from charge carriers coupling to intrinsic lattice distortions in rutile TiO_2[16] and $LiNbO_4$.[31] These self-trapping mechanisms differ from other descriptions of small polarons forming via charge carriers coupling to dopants or lattice defects.[32–35] Distinguishing the mechanism of photoinduced polaron formation (mediated by dynamic, thermally activated lattice distortions or static lattice defects) is fundamentally important to inform strategies for engineering metal oxide materials for photoapplications.

Chemical Science Accepted Manuscript

View Article Online
DOI: 10.1039/D5SC01909E

Open Access Article. Published on 12 May 2025. Downloaded on 5/16/2025 10:21:16 PM.
This article is licensed under a Creative Commons Attribution 3.0 Unported Licence.

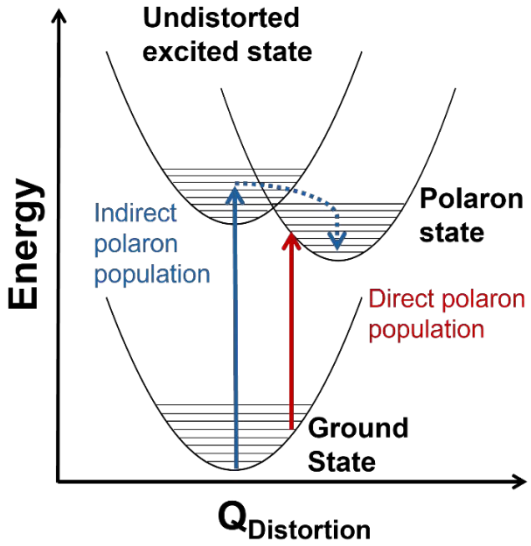

Figure 1. Conceptual configuration coordinate diagram depicting mechanisms of photoexcited polaron formation. The red arrow illustrates direct photoexcitation from a thermally distorted ground state into a polaronic state and the blue arrow shows relaxation into a polaronic state via an undistorted ground state.

Spinel oxides (AB_2O_4) offer a unique opportunity to understand how the mechanism of photoinduced polaron formation depends on orbital composition of the band edge, coordination geometry of metal centers, and the presence of substitutional defects. These materials are mixed-valent with $Fd\bar{3}m$ symmetry and two different site symmetries for metals: tetrahedral (T_d) and octahedral (O_h). Ternary spinel oxides, in which A and B are different metals, are described by an inversion parameter x ($0.0 < x < 1.0$) that quantifies the percent of the A cations that occupy octahedral sites. When x = 0.0, meaning all of the A cations are in tetrahedral sites, the spinel is considered "normal," whereas when x = 1.0, meaning all of the A cations are in octahedral sites, the spinel is fully inverted. Intermediate values of x correspond to population of A cations in both tetrahedral and octahedral sites. Spinel oxides containing cobalt are of particular interest because of the difference in crystal field splittings of Co^{2+} T_d and Co^{3+} O_h (Figure 1A). Transitions between the *e* and t_2 states within the T_d sites are allowed by the Laporte selection rule whereas this rule forbids transitions between the t_{2g} and e_g states within the O_h sites. Normal Co_3O_4, which contains both Co^{2+} T_d and Co^{3+} O_h, exhibits optical transitions associated with localized *d-d* transitions at 0.8, 0.9 and 1.6 eV, in addition to an optical transition at 2.5 eV associated with a ligand-to-metal-charge transfer (LMCT) transition.[36–40] Normal $ZnCo_2O_4$, with only Co^{3+} O_h, is reported to have only the LMCT-type transition at 2.5 eV.[27] The coordination geometry of cobalt in spinel oxides thus impacts their optical spectra; we aim to understand how this coordination geometry impacts photoinduced polaron formation.

The formation of small polarons in Co spinel oxides (Co_3O_4 and $ZnCo_2O_4$) has been inferred from the observation of thermally activated charge transport in these materials;[26,27] however, as with other transition metal oxides, descriptions of photoinduced polarons in these materials are scarce. Transient absorption (TA) studies

Chemical Science Accepted Manuscript

View Article Online
DOI: 10.1039/D5SC01909E

Open Access Article. Published on 12 May 2025. Downloaded on 5/16/2025 10:21:16 PM.
This article is licensed under a Creative Commons Attribution 3.0 Unported Licence.

of Co_3O_4 have reported that the strongest TA signal is induced by thermal effects,[41,42] which mirrors the behavior of hematite, a material known to undergo photoinduced polaron formation.[29,30,43,44] In other work using extreme ultraviolet (XUV) spectroscopy, Zhang, *et al.* describe indirect formation of small polarons from self-trapped photocarriers in Co_3O_4.[45] Using a combined approach of resonance Raman spectroscopy, temperature-dependent optical spectroscopy and Hubbard-corrected density functional theory, we investigate the influence of cobalt coordination geometry on photoinduced polaron formation in Co_3O_4 and $ZnCo_2O_4$. We report evidence of T_d Co in Co_3O_4 mediating resonance Raman enhancement of specific phonon modes, indicating the presence of phonon-coupled optical transitions that lead to polaron formation. Parallel studies of partially inverted $ZnCo_2O_4$, in which the majority of the T_d Co ions are replaced with Zn, confirm the involvement of T_d Co in phonon-coupled transitions; however, in $ZnCo_2O_4$ these transitions do not depend on temperature, suggesting that the polarons form at static defects rather than dynamic lattice distortions. The fundamental understanding of photophysical properties as a function of coordination geometry presented here is crucial to designing transition metal oxides for optical applications.

RESULTS AND DISCUSSION

Assignment of the Optical Spectra of Co_3O_4

Co_3O_4 adopts a spinel crystal structure (space group $Fd\bar{3}m$) with two different metal sites: Co^{3+} ions occupy octahedral sites and Co^{2+} ions occupy tetrahedral sites (Figure 1A). The two coordination sites give rise to two distinct crystal field splittings of the 3*d* orbitals as shown in Figure 1A. Transitions between the *e* and t_2 states within the T_d sites are allowed by the Laporte selection rule whereas this rule forbids transitions between the t_{2g} and e_g states within the O_h sites. The unpaired electrons of adjacent T_d Co^{2+} atoms in Co_3O_4 are antiferromagnetically coupled.[46] Density Functional Theory with Hubbard and Hund corrections (DFT+*U*+*J*) was used to calculate the ground-state electronic structure of Co_3O_4 within the Born-Oppenheimer approximation, in which nuclear motion is neglected. Hubbard (electron correlation correction)[47] and Hund (local magnetization correction)[48] corrections are used in highly correlated materials such as Co_3O_4 to mitigate self-interaction errors.[30] Using a linear response method,[30,47] *U* and *J* parameters were calculated for Co_3O_4 from first principles via perturbation of the local environments of open-shell ions (T_d $Co^{2+}$and O_h Co^{3+} in the case of Co_3O_4, see Supporting Information for more computational details). From the DFT+*U*+*J*-computed band structure and projected density of states (pDOS) shown in Figure 1B, *3d* orbitals associated with Co^{2+} T_d atoms are the primary contributors to an energetically isolated band at the valence band maximum (VBM), whereas both Co^{2+} T_d and Co^{3+} O_h 3*d* orbitals contribute to the conduction band minimum (CBM). These computed results suggest isolated valence bands with Co^{2+} T_d character participate in the low-energy transitions observed in the experimental imaginary dielectric spectrum at 0.82 and 0.92 eV (labeled a, b in Figure 1C).

Chemical Science Accepted Manuscript

View Article Online
DOI: 10.1039/D5SC01909E

Open Access Article. Published on 12 May 2025. Downloaded on 5/16/2025 10:21:16 PM.
This article is licensed under a Creative Commons Attribution 3.0 Unported Licence.

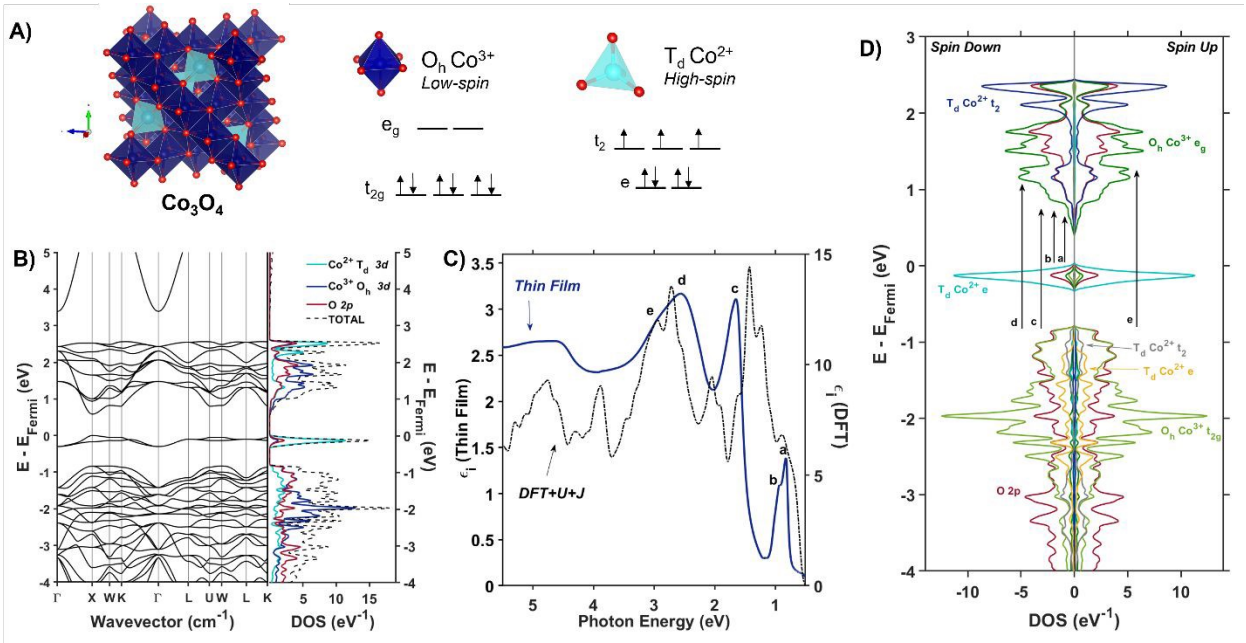

Figure 2. (A) The Co_3O_4 unit cell ($Fd\bar{3}m$) with associated *d*-splitting diagrams for Co^{3+} (O_h) and Co^{2+} (T_d). **(B)** Electronic band structure and projected density of states calculated with Hubbard-corrected DFT. **(C)** Plot of experimentally (solid blue line) and computationally (dashed black line) determined imaginary dielectric spectra of Co_3O_4. Labels a-e correlate with arrows in **(D),** the spin-symmetrized projected density of states arising from the primitive cell of Co_3O_4.

Figure 1C plots the DFT+*U*+*J*-computed dielectric spectrum overlaid with the experimental dielectric spectrum extracted from transmission and reflection spectra measured from a 53.7-nm thick Co_3O_4 film (see SI for details of dielectric spectrum determination and powder X-ray diffraction pattern). We applied a rigid shift of +0.3 eV to all conduction band eigenvalues to bring the computed dielectric function into alignment with the measured spectrum. Herein, this shift is applied to all electronic band diagrams and electronic density of states plots of Co_3O_4. In order to fulfill the *f*-sum rule governing total oscillator strength, all computed optical spectra are subsequently renormalized by a factor of $(1- (0.3\ \text{eV} / \hbar\omega))$.[49,50] The computed single-particle dielectric spectrum shows good agreement with the measured spectrum, confirming the features at 0.82, 0.92 and 1.64 eV involve Co^{2+} T_d bands (a-c). From the spin-resolved density of states separated into band contributions from t_{2g} and e_g (O_h), *e* and t_2 (T_d) and O 2*p* (Figure 2D), optical transitions are assigned while also considering spatial wavefunction overlap. The onsets of the conduction bands derived from O_h Co^{3+} e_g, T_d Co^{2+} t_2, and O 2*p* occur at the same energy; however, the highest projected density of states comes from O_h Co^{3+} e_g. Thus, when considering transitions from T_d Co^{2+} *e* to the conduction band, these DFT+*U*+*J* computations exhibit no energetic difference among transitions to O_h Co^{3+} e_g, T_d Co^{2+} t_2, and O 2*p*. The oscillator strength of the experimental dielectric peak at 0.82 eV is higher than the 0.92 shoulder, indicating the higher likelihood of the transition; however, the shoulder is not resolved in the imaginary dielectric computed by DFT+*U*+*J*. Therefore, to assign this shoulder, we qualitatively assessed the spatial overlap of orbital wavefunctions by mapping the contributions of specific atoms to specific projected

Chemical Science Accepted Manuscript

View Article Online
DOI: 10.1039/D5SC01909E

Open Access Article. Published on 12 May 2025. Downloaded on 5/16/2025 10:21:16 PM.
This article is licensed under a Creative Commons Attribution 3.0 Unported Licence.

densities of states (Figure S10). This approach reveals that the most probable transition contributing to the 0.82 eV feature is an intra-atomic transition of Co^{2+} T_d that satisfies the spin transition selection rule (Figure S10A, B). The spatial overlap of the orbitals involved in an intra-atomic transition is greater than the overlap of orbitals between a T_d Co and an O_h Co (inter-sublattice charge transfer), leading to the assignment of the 0.82 eV optical transition to an intra-atomic *d*-to-*d* transition in T_d Co^{2+} ($e \rightarrow t_2$). From the spin-resolved density of states combined with our spatial overlap analysis, the feature at 0.92 eV is described by a charge transfer from the tetrahedral sublattice to the octahedral sublattice (T_d Co^{2+} $e \rightarrow O_h$ Co^{3+} e_g). Similarly, the transition at 1.62 eV can be described as an inter-sublattice charge transfer from O_h Co^{3+} $t_{2g} \rightarrow T_d$ Co^{2+} t_2. The covalency between T_d Co^{2+} and O 2*p*, as well as O_h Co^{3+} and O 2*p*, allows these metal-to-metal (inter-sublattice charge transfer) transitions to occur. The feature at 2.55 eV and its shoulder at 2.90 eV arise from ligand-to-metal charge transfer (LMCT) type transitions. The assignment of these two LMCT transfers is resolved from comparing the experimental spectrum of Co_3O_4 with $ZnCo_2O_4$, which has majority O_h Co^{3+} (Figure S12). It becomes apparent that the O 2*p* $\rightarrow$ O_h Co^{3+} e_g transition is slightly higher in energy than the O 2*p* $\rightarrow$ O_h Co^{2+} t_{2g}, leading to the following assignments: O 2*p* $\rightarrow$ T_d Co^{2+} t_2 (2.55 eV) and O 2*p* $\rightarrow$ O_h Co^{3+} e_g (2.90 eV). All transitions are spin-conserved (Figure 1D, Table 1).

Table 1. Assignment of Optical Transitions in Co_3O_4

Peak Center (eV)	Label	Transition	Description
0.82	a	T_d Co^{2+} $e \rightarrow t_2$	Intra-atomic transition
0.92	b	T_d Co^{2+} $e \rightarrow O_h$ Co^{3+} e_g	Inter-sublattice charge transition
1.64	c	O_h Co^{3+} $t_{2g} \rightarrow T_d$ Co^{2+} t_2	Inter-sublattice charge transition
2.55	d	O 2*p* $\rightarrow$ T_d Co^{2+} t_2	Ligand-to-metal charge transition
2.90	e	O 2*p* $\rightarrow$ O_h Co^{3+} e_g	Ligand-to-metal charge transition

The electronic density of states and band structures of Co_3O_4 have been previously calculated with many approaches including, but not limited to GGA+*U,* hybrid functional PBE0, range-separated exchange–correlation functional HSE06, and many-body Green's function GW approximation.[27,51,52] Commonly, the density of states shows some degree of Co 3*d* and O 2*p* wavefunction overlap at the band edges; however, depending on the computational approach, the band gap varies from 0.78 to 1.6 eV.[27,51,52] Singh *et al*. explored many different DFT approaches to calculating the electronic structure of Co_3O_4, including PBE, PBE+U_{eff}, HSE06, and many-body Green's function using the GW approximation (Sc-GW0).[52] Of these, the Sc-Gw0 method produces the most accurate representation of the electronic structure of Co_3O_4 based on computed electronic bands, density of states, and absorption spectra.[52] Although the absorption spectrum computed with Sc-GW0 exhibits a high oscillator strength between ~0.5 and 2.0 eV,[52] unlike our DFT+*U*+*J* approach, it cannot resolve the two distinct transitions at 0.8 and 1.6 eV reported in experimental optical spectra.[27,36,37,41,45]

The experimental presence of the 0.8-eV optical transition and discrepancies of the band gaps computed with various approaches has led to debate over defining the

Chemical Science Accepted Manuscript

View Article Online
DOI: 10.1039/D5SC01909E

Open Access Article. Published on 12 May 2025. Downloaded on 5/16/2025 10:21:16 PM.
This article is licensed under a Creative Commons Attribution 3.0 Unported Licence.

optical band gap of Co_3O_4: some report it as 0.8 eV, [27,39,53] while others define the band-gap as 1.6 eV.[41,54] The incongruity in reported band gap values is scrutinized by Smart, *et al*. in their work modelling Co_3O_4 optical transitions with DFT+*U* and a hybrid functional that includes a fraction of Hartree-Fock exchange. They propose the 0.8-eV optical transition arises from photoinduced formation of a small hole polaron that becomes most apparent upon application of uniaxial lattice strain.[55] Our calculation of the ground-state electronic structure of Co_3O_4 using a Hubbard- and Hund- corrected plane-wave pseudopotential approach demonstrates that the low-energy transition at 0.8 eV (and its 0.9-eV shoulder) arise from localized Co^{2+} T_d bands. Additionally, the corresponding empty Co^{2+} T_d conduction bands (t_2) participate in the observed transition at 1.64 eV, indicating the importance of T_d Co^{2+} electronic character to this transition as well. Although the computational approach used here is a single-particle method that neglects many-body perturbations and nuclear motion, its ability to capture all the features observed in the experimental dielectric spectrum supports its accuracy in describing the nature of the bands that contribute to optical transitions in Co_3O_4. Because the dielectric spectrum reported here is calculated within the Born-Oppenheimer approximation, transitions originating from ground states containing nuclear displacements are not captured, contrasting the description of the 0.8 eV transition as involving a lattice strain-induced small hole polaron by Smart, *et al.*[55]

Optical phonon enhancement in Co_3O_4

We assess phonon coupling to various optical transitions in Co_3O_4 using resonance Raman spectroscopy. Figure 2A plots a series of resonance Raman spectra collected for a 428-nm thick Co_3O_4 film deposited on a sapphire substrate using a variety of excitation lasers with photon energies ranging from 1.49 to 3.06 eV, which spans the Co_3O_4 absorption spectrum (Figure 2B). These Raman spectra of Co_3O_4 each contain five phonon modes, consistent with previous reports.[56,57] The phonon mode at 86 meV (oxygen breathing about T_d Co^{2+}, Figure 3D) is the most intense at all excitation energies, except $h\nu_{exc}$ = 1.88 eV, which corresponds to the inter-sublattice charge transfer transition (O_h Co^{3+} $e_g \rightarrow T_d$ Co^{2+} t_2). When Co_3O_4 is excited with a photon energy of 1.58 eV, which correspond to the lower-energy edge of this inter-sublattice charge transfer peak, the 86-meV phonon mode becomes most intense again. Figure 2C plots the excitation spectrum for each phonon mode corrected for scattering cross section and sample absorption, which enables the comparison of phonon mode intensities across different excitation energies. This quantitative analysis of relative intensities reveals that there is amplified resonance enhancement of all modes upon excitation at 1.49 eV, indicating strong phonon coupling to this optical transition. This analysis was repeated on a thin film of Co_3O_4 deposited on quartz, and the same trends are apparent (Figure S7). Given that the 86-meV phonon mode is most intense at an excitation energy of 1.49 eV, we propose it is this phonon mode that most strongly couples to the optical transition at 1.49 eV.

Chemical Science Accepted Manuscript

View Article Online
DOI: 10.1039/D5SC01909E

Open Access Article. Published on 12 May 2025. Downloaded on 5/16/2025 10:21:16 PM.
This article is licensed under a Creative Commons Attribution 3.0 Unported Licence.

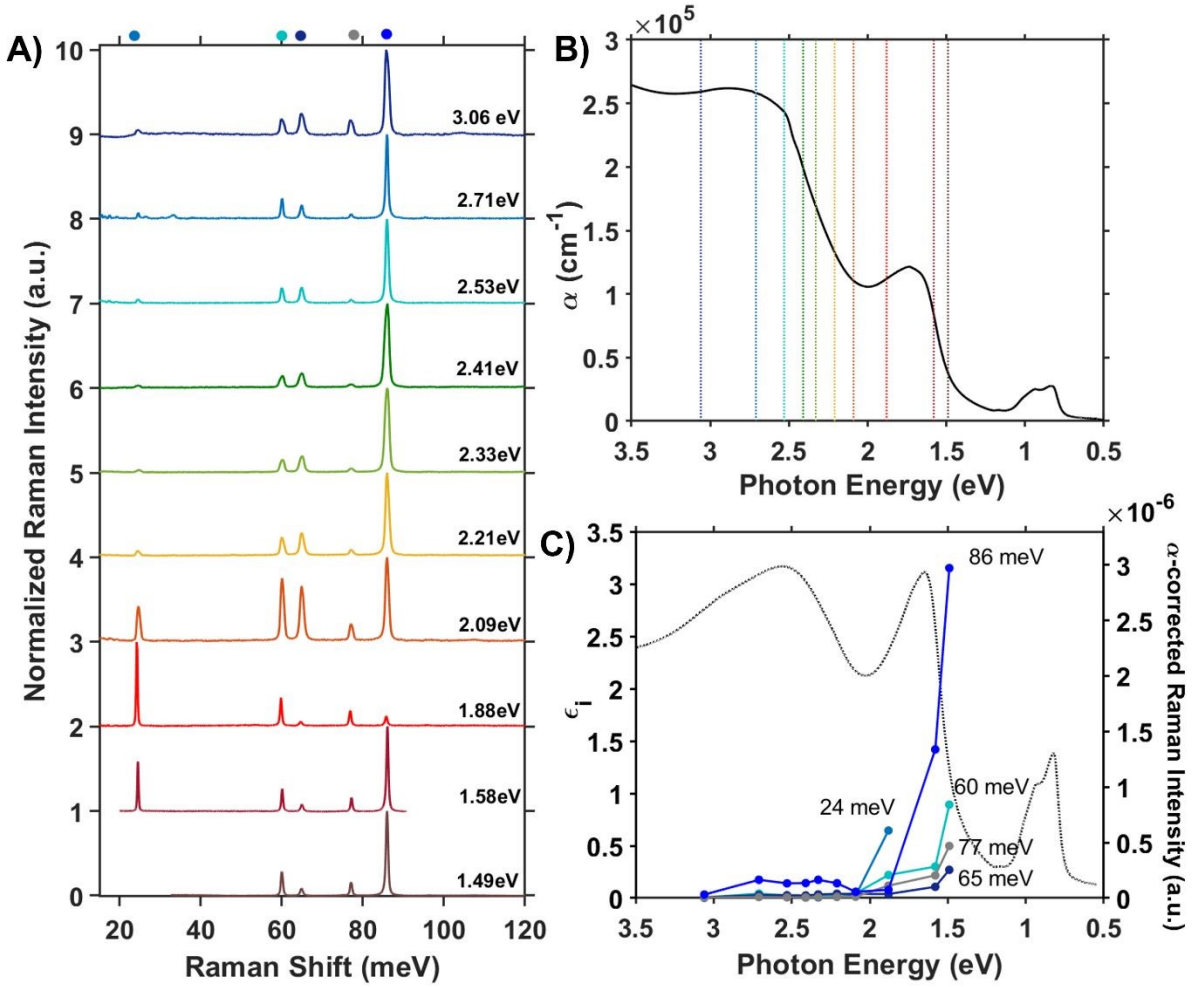

Figure 3: (A) Internally normalized Raman spectra of Co_3O_4 collected with various excitation energies that span the absorption spectrum plotted in **(B)**. Raman spectra are vertically offset for clarity. Because the spectra are internally normalized, only relative changes in phonon mode intensity can be assessed as a function of excitation energy. Note that the spectrum excited with 1.49 eV begins at a Raman shift of 30 meV due to instrumental constraints, primarily the bandwidth of the filter used to remove Rayleigh scattering. **(C)** Plot of the intensities of the various Raman modes shown in part **A** corrected for scattering cross section and sample absorption superimposed on the imaginary dielectric spectrum. Note the corresponding color point of each phonon mode indicated above the relevant Raman peak in **A**. For the full correction, see Supporting Information Figure S5.

DFT+*U*+*J* was used to calculate the displacement vectors of all 39 optical phonon modes in Co_3O_4 at k-point Γ (Table S2). White and DeAngelis determined through evaluating the Raman selection rules that there are five Raman active modes in normal spinel oxides.[58] The symmetry of these modes was compared with the displacement vectors computed with DFT+*U*+*J* to identify the Raman active modes, the energies of which are overlaid with the Raman spectrum in Figure 3A. From the resonance Raman profile (Figure 2A, C), the phonon modes with energies of 24, 60, and 86 meV exhibit the most significant resonance enhancement upon excitation at 1.49 eV, corresponding to

Chemical Science Accepted Manuscript

View Article Online
DOI: 10.1039/D5SC01909E

Open Access Article. Published on 12 May 2025. Downloaded on 5/16/2025 10:21:16 PM.
This article is licensed under a Creative Commons Attribution 3.0 Unported Licence.

the onset of the absorption feature centered at 1.64 eV. These modes correspond to motion of tetrahedral Co^{2+} (24 meV), octahedral Co^{3+} (60 meV), and oxygen stretching symmetrically about Co^{2+} T_d atoms (Figure 3B-D).

The observed enhancement of the 24-meV (T_d Co^{2+}motion) and 60-meV (O_h Co^{3+} motion) phonons at 1.49 eV is related to the contribution of both T_d Co^{2+} and O_h Co^{3+} electronic character to this optical transition, which corresponds to population of empty T_d Co^{2+} t_2 conduction band states from O_h Co^{3+} e_g valence band states. Although both T_d Co^{2+} and O_h Co^{3+} phonon modes exhibit resonance enhancement because of associated electronic character in the optical transition centered at 1.64 eV, it is the oxygen breathing mode about Co^{2+} T_d ions at 86 meV that exhibits the most enhancement. The degree of energetic overlap between the O 2*p* and Co^{2+} T_d projected density of states in the conduction band at the energy of the O_h Co^{3+} e_g $\rightarrow$$T_d$ Co^{2+} t_2 transition is significant (Figure 1B) and supports the observed enhancement of the 86-meV phonon, which corresponds to motion of oxygen atoms along their bond axes to T_d Co^{2+}.

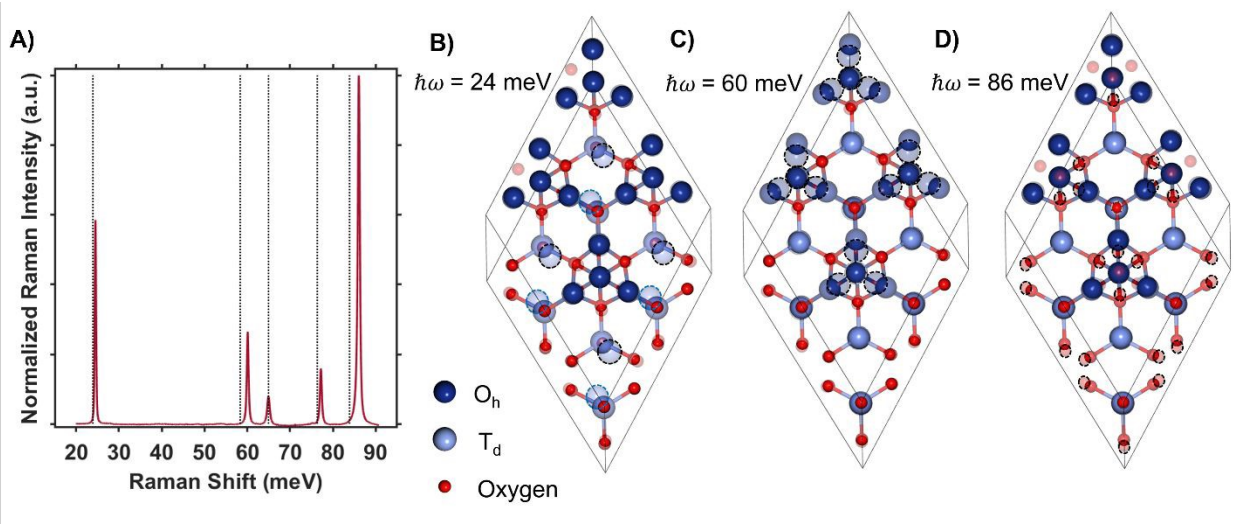

Figure 4. (A) Raman spectrum of Co_3O_4 collected with 1.58-eV excitation overlaid with DFT+*U*+*J*-computed Raman-active phonon modes. The atomic displacements corresponding to the modes at 24 meV **(B)**, 60 meV **(C)** and 86 meV **(D)** are shown. The circled atoms demonstrate the vector displacements of the phonon modes in a 2x2x1 super cell, where T_d sites are most shifted at 24 meV, O_h sites at 60 meV and oxygens surrounding T_d sites at 86 meV. Note that the extra oxygen atoms in the 24-meV and 86-meV vector-displacement images appear from the displacement of the neighboring super-cell.

Temperature dependence of optical transitions

To further understand the role of phonon-coupling in the optical transitions of Co_3O_4, we measured the dependence of its dielectric spectrum on temperature between 82-470K. Figure 4A-B plots the resulting thermal difference spectra (TDS) calculated according to equation 1. We assessed the impact of temperature on the dielectric spectrum by integrating

$$\Delta\epsilon_i(T) = \epsilon_{i,T} - \epsilon_{i,294K} \quad (1)$$

Chemical Science Accepted Manuscript

View Article Online
DOI: 10.1039/D5SC01909E

Open Access Article. Published on 12 May 2025. Downloaded on 5/16/2025 10:21:16 PM.
This article is licensed under a Creative Commons Attribution 3.0 Unported Licence.

the intensity of the thermal difference spectra. Figure 4C (blue) plots the absolute value of the thermal difference spectra integrated from 0.68–1.86 eV and normalized to the integrated intensity obtained from the spectrum collected at 82 K. To account for sign changes, the integrands of spectra collected below room temperature are shown as negative, and those above are positive. For phonon-coupled optical transitions, we expect the change in intensity with changing temperature to be proportional to the change in population of the coupled phonons. The thermal population of phonon modes is dictated by the Bose-Einstein distribution shown in equation 2, where $\hbar\Omega$ is the phonon energy. Normalization of the differential spectra to an arbitrary temperature, in this case 82 K, leads to equation 3, where we compare the change in intensity of the dielectric spectrum ($\Delta\epsilon$ defined in equation 1) to the change in population of the Raman active phonon modes at various temperatures.

$$N(\hbar\Omega,T) = \left(e^{\frac{\hbar\Omega}{kT}} - 1\right)^{-1} \times \rho(\hbar\Omega) \quad (2)$$

$$\frac{\Delta\epsilon(T)}{|\Delta\epsilon(82K)|} = \frac{N(\hbar\Omega,T) - N(\hbar\Omega,294K)}{|N(\hbar\Omega,82K) - N(\hbar\Omega,294K)|} \quad (3)$$

The temperature dependence of the TDS intensity overlays well with the change in population of the 24-meV Raman-active phonon with temperature predicted by the Bose-Einstein distribution (eq 3). This agreement suggests that the low energy optical transitions (1.64 eV, 0.96 eV and 0.82 eV) are coupled strongly to the thermal population of this phonon. Interestingly, the 24-meV phonon mode is not the most enhanced in resonance Raman spectra collected with excitation at 1.49 eV; however, both the 24-meV and 86-meV phonon modes are described by displacement vectors primarily of or around T_d Co^{2+}ions (Figure 3B). Evidence of thermally activated optical transitions combined with strong phonon coupling to optical transitions observed in resonance Raman spectra (*vide supra*) suggests an optically accessed polaronic state related to T_d Co^{2+}. Compared to resonance Raman measurements, thermal difference spectra are not as precise in determining the specific phonon modes coupling to the optical transition, as there may be multiple phonon modes contributing to thermal activation. However, the Bose-Einstein distribution corresponding to a phonon energy of 24 meV overlays the temperature-dependent TDS intensities much better than the distributions corresponding to other Raman-active phonon modes (Figure 4C). We therefore interpret the threshold phonon energy of 24 meV to be where thermal activation occurs. Similar temperature-dependent behavior is observed in α-Fe_2O_3: at the excitation energy where maximal Raman enhancement is observed (~2.2 eV), the strongest temperature-dependence in the optical spectrum is also present.[29] Thermal activation of optical transitions in α-Fe_2O_3 is the proposed mechanism by which direct excitation into intrinsic polaron states occurs.[29,30] The similarities in the trends of Raman enhancement and the temperature-dependence of the dielectric spectrum observed for Co_3O_4 and α-Fe_2O_3 support the presence of an optically accessible polaronic state in Co_3O_4 arising from coupling to intrinsic, dynamic lattice distortions (phonons) (Figure 1, red arrow).

Chemical Science Accepted Manuscript

View Article Online
DOI: 10.1039/D5SC01909E

Open Access Article. Published on 12 May 2025. Downloaded on 5/16/2025 10:21:16 PM.
This article is licensed under a Creative Commons Attribution 3.0 Unported Licence.

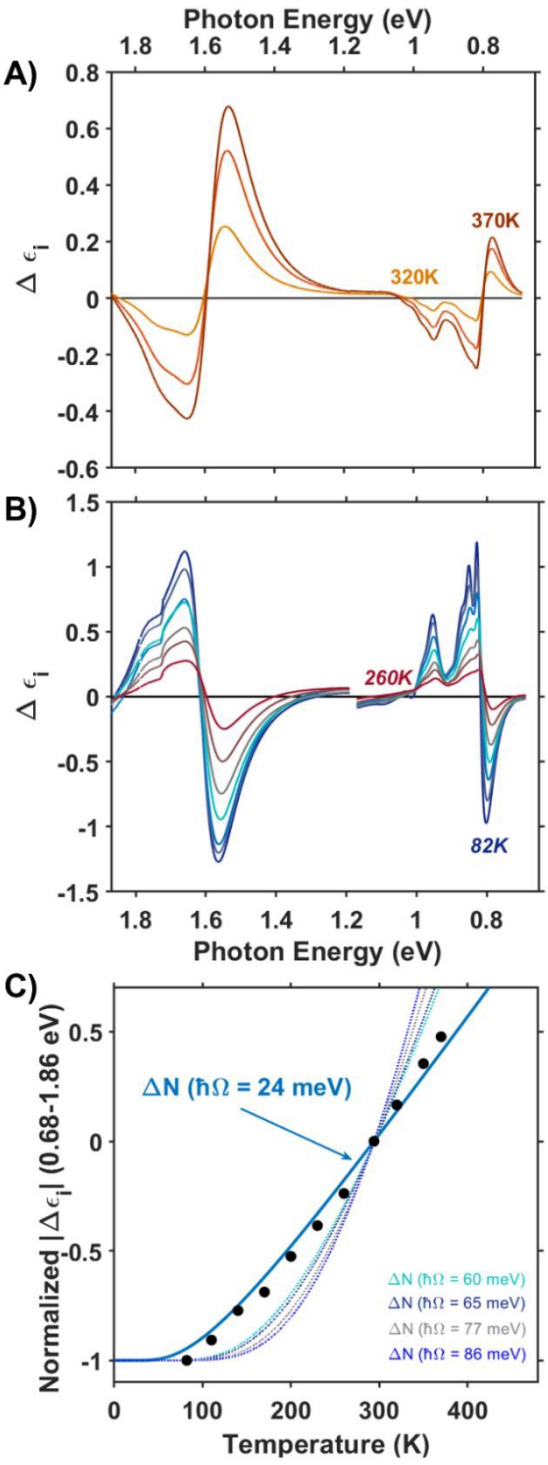

Figure 5. Thermal difference imaginary dielectric spectra of Co_3O_4 collected at temperatures above (**A**) and below (**B**) room temperature (294 K). **C**) Plot of the absolute value of the thermal difference spectra integrated from 0.68 to 1.86 eV and normalized to the integrated intensity of the spectrum collected at 82K versus temperature (black circles). The solid blue line plots the change in Bose-Einstein distribution corresponding to a phonon energy of 24 meV. Bose-Einstein distributions corresponding to the energies of the other Raman active phonon modes are plotted as dotted lines.

Chemical Science Accepted Manuscript

View Article Online
DOI: 10.1039/D5SC01909E

Open Access Article. Published on 12 May 2025. Downloaded on 5/16/2025 10:21:16 PM.
This article is licensed under a Creative Commons Attribution 3.0 Unported Licence.

Chemical Science Accepted Manuscript

Co_3O_4 compared to $ZnCo_2O_4$: assessing the role of T_d Co in spinel oxides

The resonance Raman and thermal difference spectra of Co_3O_4 suggest that Co^{2+} ions occupying T_d sites are involved in the phonon-coupled optical transitions. To further understand the role of T_d Co^{2+} in the optical spectra of Co_3O_4, we assessed the optical properties of $ZnCo_2O_4$, where Zn^{2+} replaces T_d Co^{2+}. We computed the imaginary dielectric spectrum for normal $ZnCo_2O_4$ with DFT+*U* (see SI for details). Within normal $ZnCo_2O_4$, the T_d Zn^{2+} 3*d* orbitals are completely filled, and the O_h Co^{3+} 3*d* orbitals have a low-spin configuration, termed "quasi close-shelled."[59,60] With no unpaired electrons present, the Hund parameter, *J*, is not implemented in these calculations. The DFT+*U* calculations of normal $ZnCo_2O_4$ show two absorption bands at and above ~2.5 eV, while the experimental spectrum only has one transition in this region. Literature reports assign the experimental feature at 3.0 eV to an LMCT-type transition,[27,38] which matches the lower energy peak (2.5 eV) observed in the DFT+*U* dielectric spectrum. The 3.5-eV peak in the DFT+*U* dielectric spectrum computed here is associated with an intra-sublattice charge transfer (O_h Co^{3+} t_{2g} → O_h Co^{3+} e_g). Because this is a charge transfer between two different lattice sites, the Laporte selection rule does not apply. Due to the hybridized nature of the Co *3d* and O *2p* orbitals in both the valence and conduction bands, we assign the experimental dielectric peak at 3.0 eV to a combination of LMCT and intra-sublattice charge transfer transitions (see Figure S11 in the Supporting Information). Interestingly, when comparing the experimental peak shape of the dielectric transition at 3.0 eV in $ZnCo_2O_4$ (Figure 5B) to the analogous transition in Co_3O_4 (Figure 1C, Figure S12), it becomes apparent that the shoulder in Co_3O_4 (labeled e in Figure 1C) is at the same energy as the peak center of the experimental $ZnCo_2O_4$ transition. This energetic alignment in the experimental dielectric spectra, used to assign the 2.90-eV shoulder in Co_3O_4 as excitation into O_h Co^{3+} e_g bands, has been observed previously in a Zn dopant study of Co_3O_4.[38]

The lower-energy region of the experimental dielectric spectrum of $ZnCo_2O_4$ contains broad and weak features at 1.79, 0.98 and 0.82 eV, which coincide with where Co_3O_4 has transitions associated with Co^{2+} T_d. X-ray fluorescence analysis indicates the stoichiometry of the $ZnCo_2O_4$ film used to produce the dielectric spectrum is 1.94±0.04 Co:Zn, and the powder X-ray diffraction pattern indicates the film is phase-pure spinel (Figure S3). We therefore suspected that our $ZnCo_2O_4$ film may be slightly inverted and contain a small population of cobalt in tetrahedral sites, consistent with previous reports.[61] In an effort to control cation distribution in $ZnCo_2O_4$, we changed the temperature at which $ZnCo_2O_4$ films were annealed following spin-coating. We observe that annealing above 600 °C induces phase separation as features associated with ZnO become apparent in the X-ray diffraction pattern and Raman spectra (Figure S13, S14). Additionally, as annealing temperature increases, the low energy peaks observed in the dielectric spectrum increase in intensity (Figure S15). We therefore suspect that the films containing ZnO also contain Co_3O_4, which accounts for the presence of the intense low-energy peaks in the dielectric spectrum (Figure S15). With no ZnO peaks present in X-ray diffraction or ZnO phonon modes observed in Raman for the films annealed at 600°C,

View Article Online
DOI: 10.1039/D5SC01909E

we hypothesize that the weak, low-intensity features observed in the dielectric spectra of these films arise from cation inversion, whereby a fraction of the Co ions occupy T_d sites and a fraction of the Zn ions occupy O_h sites. We describe the Co ions in T_d sites as substitutional lattice defects.

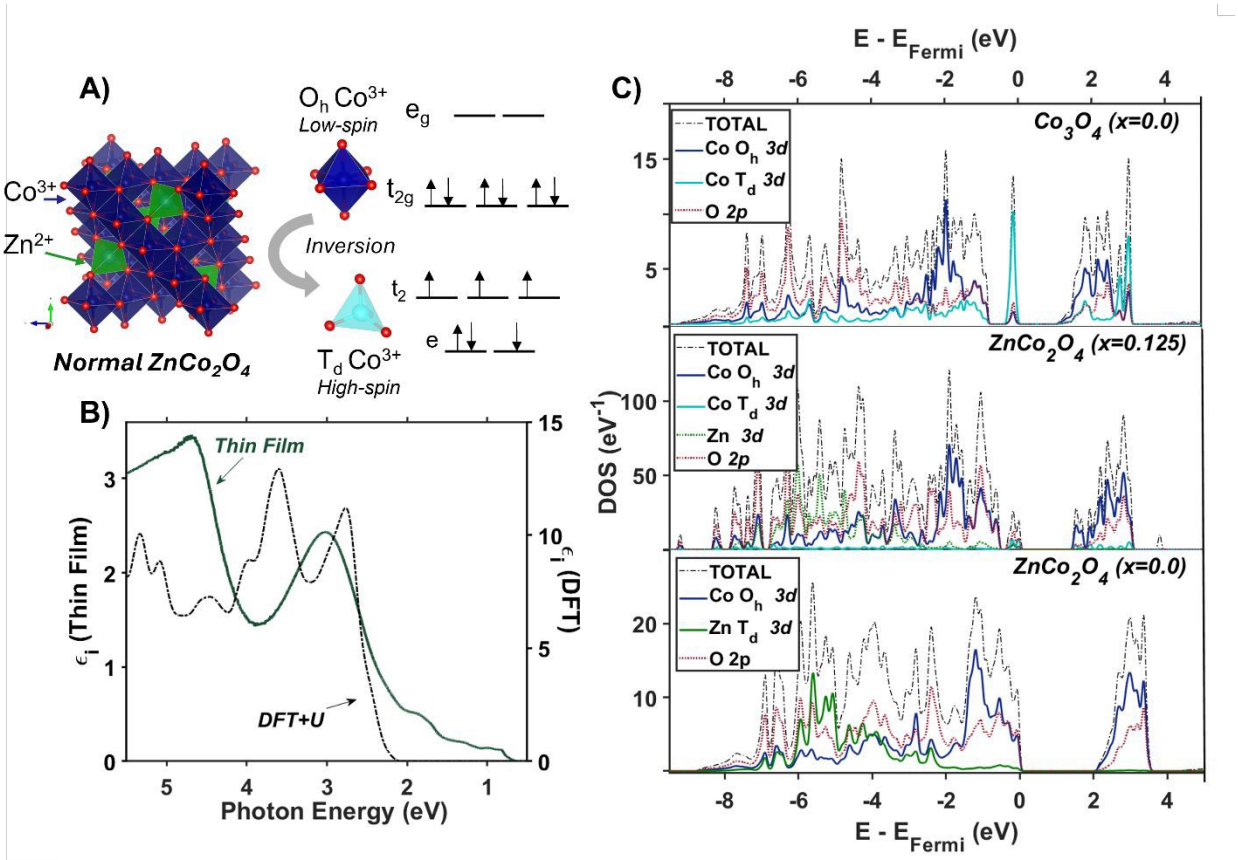

Figure 6. (A) Unit cell of normal $ZnCo_2O_4$ with associated crystal field splitting diagrams of Co^{3+} in octahedral and tetrahedral coordination. **(B)** Plot of experimentally (solid green line) and computationally (dashed black line) determined imaginary dielectric spectra of $ZnCo_2O_4$. The computed dielectric spectrum was calculated for normal $ZnCo_2O_4$. **(C)** The electronic density of states calculated with Hubbard-corrected DFT for normal Co_3O_4 (top), $ZnCo_2O_4$ with an inversion factor of 0.125 (middle), and normal $ZnCo_2O_4$ (bottom).

To investigate the impact of cation inversion on the optical spectra of $ZnCo_2O_4$, we computed the electronic structure of inverted $ZnCo_2O_4$ using Hubbard-corrected DFT (see Supporting Information for details). Inverted $ZnCo_2O_4$ (i-$ZnCo_2O_4$) was modeled by switching two O_h Co^{3+} ions with two T_d Zn^{2+} ions within a 2x2x2 supercell of normal $ZnCo_2O_4$ to produce an inversion factor of x = 0.125 while maintaining charge balance and stoichiometry. The resulting two T_d Co^{3+} ions were modeled to be antiferromagnetically coupled to maintain net-zero magnetization. Compared to normal $ZnCo_2O_4$ (n-$ZnCo_2O_4$), i-$ZnCo_2O_4$ contains an isolated state at the valence band-edge with primarily T_d Co and O 2*p* character (Figure 5D, middle and bottom). The conduction

Open Access Article. Published on 12 May 2025. Downloaded on 5/16/2025 10:21:16 PM.
This article is licensed under a Creative Commons Attribution 3.0 Unported Licence.

Chemical Science Accepted Manuscript

View Article Online
DOI: 10.1039/D5SC01909E

band edge in i-$ZnCo_2O_4$ appears at a lower energy than that in n-$ZnCo_2O_4$ (similar to Co_3O_4), and i-$ZnCo_2O_4$ contains an isolated region at the conduction band-edge of primarily O_h Co and O 2*p* character (Figure 5D, middle and top). The band-edge character of i-$ZnCo_2O_4$, despite the 3+ oxidation state of the cobalt ion in T_d sites, has more similarities to that of Co_3O_4 than n-$ZnCo_2O_4$ (Fig 5D). Thus, the presence of Co (T_d) in spinel oxides results in low-energy *d*-to-*d* transitions, regardless of its oxidation state (2+ or 3+). Because there is no evidence of phase separation (i.e presence of Co_3O_4) to describe the low-energy features in the dielectric, we conclude the synthesized $ZnCo_2O_4$ contains at least a small degree of inversion.

The Raman spectrum of $ZnCo_2O_4$ has five distinct modes (Figure 6A, B) consistent with previous reports.[62,63] The phonon mode frequencies are similar to those observed in Co_3O_4, which is expected, as both materials adopt the spinel crystal structure. Additionally, the 23-meV, 61-meV, and 89-meV phonon modes in $ZnCo_2O_4$ are described by the same phonon motions as in Co_3O_4: T_d, O_h, and oxygen stretching about T_d sites respectively (Figure 3B-D). Figure 6B (top) plots the experimental Raman spectrum of $ZnCo_2O_4$ overlaid with the computed phonon modes of normal $ZnCo_2O_4$. While the five prominent phonon modes are accounted for by DFT+*U* phonon calculations, there are two broad and weak features at 26-meV and 85-meV that do not appear in calculations. Both phonons have similar energies to corresponding modes observed in Co_3O_4, which are both related predominantly to T_d sites (Figure 6B, bottom). The discrepancy between the experimental observation of Raman-active optical phonon modes and the computed modes of normal $ZnCo_2O_4$ can be explained by the sample crystallizing with a degree of inversion. With a small percentage of tetrahedral sites occupied by Co^{3+}, and the rest by Zn^{2+}, the phonon modes dominated by tetrahedral motion (~24 meV and ~89 meV) split into two distinct distributions. This phenomenon has been observed in other inverted spinel oxides[64] and is further evidence of the $ZnCo_2O_4$ films crystallizing with a small percent occupation of cobalt in tetrahedral sites.

Open Access Article. Published on 12 May 2025. Downloaded on 5/16/2025 10:21:16 PM.
This article is licensed under a Creative Commons Attribution 3.0 Unported Licence.

Chemical Science Accepted Manuscript

View Article Online
DOI: 10.1039/D5SC01909E

Open Access Article. Published on 12 May 2025. Downloaded on 5/16/2025 10:21:16 PM.
This article is licensed under a Creative Commons Attribution 3.0 Unported Licence.

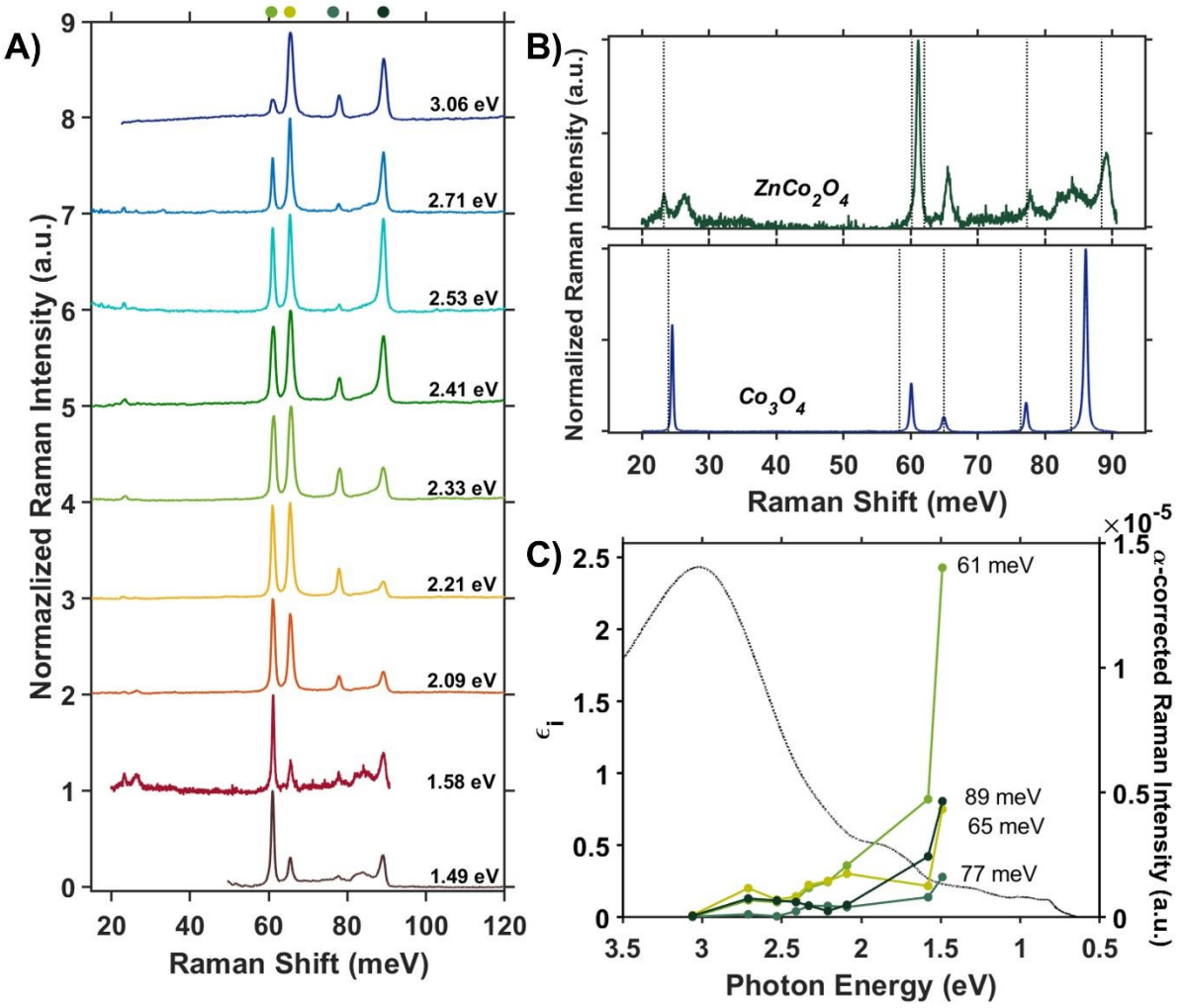

Figure 7. (A) Internally normalized Raman spectra of a $ZnCo_2O_4$ deposited on a sapphire substrate collected with excitation energies across its absorption spectrum. Because the spectra are internally normalized, only relative changes in phonon mode intensity can be assessed as a function of excitation energy. (See Supporting Information for full work-up of Raman data) **(B)** Raman spectra of $ZnCo_2O_4$ (top) and Co_3O_4 (bottom) excited at 1.58 eV excitation are overlaid with the Raman-active phonon modes computed for normal $ZnCo_2O_4$ and Co_3O_4, respectively. **(C)** Plot of the intensities of the various Raman modes shown in part **A** corrected for scattering cross section and sample absorption superimposed on the imaginary dielectric spectrum of $ZnCo_2O_4$. Note the corresponding color point of each phonon mode indicated above the relevant Raman peak in **A**.

Unlike Co_3O_4, the resonance Raman profile of $ZnCo_2O_4$ does not exhibit increased resonance enhancement of the phonons associated with T_d motion (23 and 89-meV) with decreasing excitation energy. In contrast, the 61-meV phonon, related to Co O_h motion (described by Figure 3B), exhibits enhanced intensity in $ZnCo_2O_4$ relative to all the other modes with decreasing excitation energy (Figure 6A). Interestingly, when the Raman profile is corrected for scattering cross section and sample absorption, the 61-meV mode is most enhanced at an excitation photon energy of 1.49 eV - the same excitation photon energy at which the most significant resonance enhancement was observed in Co_3O_4

Chemical Science Accepted Manuscript

View Article Online
DOI: 10.1039/D5SC01909E

Open Access Article. Published on 12 May 2025. Downloaded on 5/16/2025 10:21:16 PM.
This article is licensed under a Creative Commons Attribution 3.0 Unported Licence.

(Figures 6C, 2C). This analysis was repeated on a thin film of $ZnCo_2O_4$ deposited on quartz, and the same trends are apparent (Figure S8). The similarity in excitation energy where resonance enhancement is observed in $ZnCo_2O_4$ and Co_3O_4 indicates that the onset of the optical transition centered at ~1.6 eV is significant for both materials.

Based on the calculated density of states of inverted $ZnCo_2O_4$ (Figure 5D), the experimental optical transition observed at 1.6 eV is assigned to metal-to-metal charge transfer (MMCT) from bands with T_d Co^{3+} character (arising from the T_d Co substitutional defects) to bands with O_h Co^{3+} character. The most enhanced Raman spectrum (E_{exc}=1.49 eV) occurs upon excitation at the onset of the 1.6-eV transition, implying that the presence of the Co^{3+} T_d substitutional defect is crucial for the observed enhancement of the O_h phonon in $ZnCo_2O_4$. The conduction band character associated with the 1.6-eV transition arises from 3*d* orbitals associated with Co^{3+} O_h, the same site associated with the main vibrational motion of the 61-meV phonon (Figure 3B). Although the strong resonance enhancement observed for the 61-meV phonon in $ZnCo_2O_4$ is evidence of strong coupling between this mode and the optical transition at 1.6 eV, we do *not* observe significant temperature dependence of this transition in thermal difference spectra when compared to Co_3O_4 (see Figure S16 in Supporting Information). In fact, unlike Co_3O_4, the thermal difference spectra collected for $ZnCo_2O_4$ at elevated temperatures do not exhibit any well-defined features corresponding to spectral features observed in the dielectric spectrum at room temperature.

The spectral and computational results reported here for $ZnCo_2O_4$ and Co_3O_4 indicate that Co 3*d* character at the band edge mediates phonon-coupled optical transitions (Figures 2C, 3B, 6B). However, the contrast in temperature-dependence of the optical transition where both materials exhibit the strongest phonon coupling (1.6 eV) suggests fundamentally different processes dictating the observed enhancement. We interpret our findings in Co_3O_4 as direct population of an intrinsic polaronic state via photoexcitation, which is strongly influenced by the contributions of Co^{2+} T_d ions to the band-edge states. In $ZnCo_2O_4$, we interpret the experimental $ZnCo_2O_4$ sample to have a small percent occupation of tetrahedral sites by Co based on the presence of low energy optical transitions associated with T_d Co. Although the occupation of Co^{3+} in tetrahedral sites allows the optical transition and phonon enhancement at 1.6 eV, the lack of significant temperature dependence of this optical transition indicates that the phonon-coupled optical transitions leading to Raman enhancement in $ZnCo_2O_4$ are fundamentally different from those observed in Co_3O_4.

We suspect that the differences observed in the thermal difference spectra of Co_3O_4 and $ZnCo_2O_4$ are related to the disruption in the translational symmetry of the lattice induced by cation inversion in $ZnCo_2O_4$. From assignment of optical transitions in Co_3O_4, the low-energy optical transitions are either highly localized transitions between neighboring Co atoms or intra-atomic transitions in T_d Co (Table 1). With fewer Co atoms in T_d sites, these optical transitions become suppressed, as observed in $ZnCo_2O_4$ (Figure 5B); however, the localized transitions still exhibit phonon coupling, leading to the observed resonance Raman enhancements (Figure 6C). The lack of temperature dependence of these transitions in $ZnCo_2O_4$ suggests that, although these transitions

Chemical Science Accepted Manuscript

View Article Online
DOI: 10.1039/D5SC01909E

Open Access Article. Published on 12 May 2025. Downloaded on 5/16/2025 10:21:16 PM.
This article is licensed under a Creative Commons Attribution 3.0 Unported Licence.

access localized phonon-coupled states, the localization is related to the static lattice defect of tetrahedral cobalt rather than thermally induced dynamic lattice displacements within a pristine, translationally symmetric lattice. The lack of thermal dependence in $ZnCo_2O_4$, but presence of resonance Raman enhancement of O_h phonon modes upon excitation of a transition from T_d Co to O_h Co, is strong evidence of an optically accessed polaronic state. We therefore conclude that in both Co_3O_4 and $ZnCo_2O_4$ there is evidence of an optically accessible polaronic state. However, in Co_3O_4 formation of the polaronic state is due to intrinsic, dynamic lattice deformations caused by thermally activated phonons (exactly analogous to the mechanism we observe in hematite), whereas in $ZnCo_2O_4$ photoinduced polaron formation is mediated by static lattice defects arising from cation inversion.

CONCLUSIONS

The optical characterization of Co_3O_4 and $ZnCo_2O_4$ reported here shows that low energy transitions at 0.8, 0.9 eV and 1.6 eV arise from tetrahedrally coordinated cobalt ions, regardless of oxidation state (Co^{2+}, Co^{3+}). The *d-d* transition at 1.6 eV in both Co_3O_4 and $ZnCo_2O_4$ is a phonon-coupled optical transition. In Co_3O_4, the combination of temperature dependence and resonance enhancement at the onset of the O_h $Co^{3+} \rightarrow T_d$ Co^{2+} optical transition (1.64 eV) is evidence that this transition directly populates an intrinsic polaron state coupled to thermally activated phonons. Although the resonance Raman profile of $ZnCo_2O_4$ exhibits a similar Raman enhancement upon excitation of the 1.6 eV transition, the observed inversion and lack of temperature dependence suggests that this photoexcited polaron forms due to the presence of tetrahedral cobalt substitutional defects within the lattice. We conclude T_d-coordinated cobalt is a significant factor in phonon-coupled transitions for cobalt-containing spinel oxides. The contrast in the mechanism of polaron formation (intrinsic or self-trapped polaron vs. defect-mediated polaron) observed for these similar materials is an important insight that we anticipate will help uncover mechanisms of photoinduced polaron formation in other oxide materials. Although both mechanisms of polaron formation observed here have been previously reported, understanding the spectral signatures that distinguish them is crucial for further development of oxide materials for photo-applications.

AUTHOR CONTRIBUTIONS

E.P.C., J.L.S., and K.E.K. contributed to conceptualization of the project and interpretation of the data; K.E.K. supervised the project. E.P.C. performed most experiments and computations. J.L.S. contributed to some computations for Co_3O_4. M.T.R. collected low-frequency Raman spectra. E.P.C. wrote the manuscript. All authors reviewed the manuscript.

CONFLICTS OF INTEREST

There are no conflicts to declare.

Chemical Science Accepted Manuscript

View Article Online
DOI: 10.1039/D5SC01909E

Open Access Article. Published on 12 May 2025. Downloaded on 5/16/2025 10:21:16 PM.
This article is licensed under a Creative Commons Attribution 3.0 Unported Licence.

DATA AVAILABILITY

Data supporting this article have been included as part of the ESI. Primary data are available from the authors upon reasonable request.

ACKNOWLEDGMENTS

Financial support for this work was provided by the University of Rochester via a University Research Award. The authors acknowledge the University of Rochester Raman Facility and thank David McCamant for discussion about Raman collection. We are grateful to the computational resources and technical assistance from the University of Rochester Center for Integrated Research Computing. For X-ray diffraction and energy dispersive X-ray emission measurements, we acknowledge the Chemical Analysis Laboratory Material Science Facilities at Rochester Institute of Technology and thank Tom Allston for guidance on measurements. We thank Todd Krauss and URNano for access to Atomic Force Microscopes and thank Alex Searle for collection and processing of AFM data, as well as Sean O'Neil and Lisbeth Compton for discussions regarding AFM collection and work-up. We acknowledge URNano for profilometry measurements and thank Gregory Madjeski for discussions regarding data collection.

SUPPORTING INFORMATION STATEMENT

Details of experimental procedures for film fabrication and structural characterization, computational methods, additional resonance Raman spectra, thermal difference spectra of $ZnCo_2O_4$, and tables of computed phonon energies.

(1) Franchi, D.; Amara, Z. Applications of Sensitized Semiconductors as Heterogeneous Visible-Light Photocatalysts in Organic Synthesis. *ACS Sustainable Chem. Eng.* **2020**, *8* (41), 15405–15429.

(2) Luo, J.; Zhang, S.; Sun, M.; Yang, L.; Luo, S.; Crittenden, J. C. A Critical Review on Energy Conversion and Environmental Remediation of Photocatalysts with Remodeling Crystal Lattice, Surface, and Interface. *ACS Nano* **2019**, *13* (9), 9811–9840.

(3) Morin, F. J. Electrical Properties of α - Fe 2 O 3. *Phys. Rev.* **1954**, *93* (6), 1195–1199.

(4) Morin, F. J. Electrical Properties of NiO. *Phys. Rev.* **1954**, *93* (6), 1199–1204.

(5) Husek, J.; Cirri, A.; Biswas, S.; Baker, L. R. Surface Electron Dynamics in Hematite (α-Fe_2O_3): Correlation between Ultrafast Surface Electron Trapping and Small Polaron Formation. *Chem. Sci.* **2017**, *8* (12), 8170–8178.

(6) Biswas, S.; Husek, J.; Londo, S.; Baker, L. R. Ultrafast Electron Trapping and Defect-Mediated Recombination in NiO Probed by Femtosecond Extreme Ultraviolet Reflection–Absorption Spectroscopy. *J. Phys. Chem. Lett.* **2018**, *9* (17), 5047–5054.

(7) Franchini, C.; Reticcioli, M.; Setvin, M.; Diebold, U. Polarons in Materials. *Nat Rev Mater* **2021**, *6* (7), 560–586.

Chemical Science Accepted Manuscript

View Article Online
DOI: 10.1039/D5SC01909E

Open Access Article. Published on 12 May 2025. Downloaded on 5/16/2025 10:21:16 PM.
This article is licensed under a Creative Commons Attribution 3.0 Unported Licence.

(8) Landau, L. Über die Bewegung der Elektronen im Kristallgitter. *Phys Z Sowjet* **1933**, 644–645.

(9) Holstein, T. Studies of Polaron Motion. *Annals of Physics* **1959**, *8* (3), 325–342.

(10) Holstein, T. Studies of Polaron Motion. *Annals of Physics* **2000**, *281* (1–2), 725–773.

(11) Nagels, P.; Denayer, M.; Devreese, J. Electrical Properties of Single Crystals of Uranium Oxide. *Solid State Communications* **1963**, *1*, 35–40.

(12) Fröhlich, H. Electrons in Lattice Fields. *Advances in Physics* **1954**, *3* (11), 325–361.

(13) Mettan, X.; Jaćimović, J.; Barišić, O. S.; Pisoni, A.; Batistić, I.; Horváth, E.; Brown, S.; Rossi, L.; Szirmai, P.; Farkas, B.; Berger, H.; Forró, L. Tailoring Thermal Conduction in Anatase TiO_2. *Commun Phys* **2019**, *2* (1), 123.

(14) Reticcioli, M.; Diebold, U.; Kresse, G.; Franchini, C. Small Polarons in Transition Metal Oxides. In *Handbook of Materials Modeling*; Andreoni, W., Yip, S., Eds.; Springer International Publishing: Cham, 2020; pp 1035–1073.

(15) Austin, I. G.; Springthorpe, A. J.; Smith, B. A.; Turner, C. E. Electronic Transport Phenomena in Single-Crystal NiO and CoO. *Proc. Phys. Soc.* **1967**, *90* (1), 157–174.

(16) Yang, S.; Brant, A. T.; Giles, N. C.; Halliburton, L. E. Intrinsic Small Polarons in Rutile TiO_2. *Phys. Rev. B* **2013**, *87* (12), 125201.

(17) Tuller, H. L.; Nowick, A. S. Small Polaron Electron Transport in Reduced CeO_2 Single Crystals. *Journal of Physics and Chemistry of Solids* **1977**, *38* (8), 859–867.

(18) Esch, F.; Fabris, S.; Zhou, L.; Montini, T.; Africh, C.; Fornasiero, P.; Comelli, G.; Rosei, R. Electron Localization Determines Defect Formation on Ceria Substrates. *Science* **2005**, *309* (5735), 752–755.

(19) Karsthof, R.; Grundmann, M.; Anton, A. M.; Kremer, F. Polaronic Interacceptor Hopping Transport in Intrinsically Doped Nickel Oxide. *Phys. Rev. B* **2019**, *99* (23), 235201.

(20) Biswas, S.; Wallentine, S.; Bandaranayake, S.; Baker, L. R. Controlling Polaron Formation at Hematite Surfaces by Molecular Functionalization Probed by XUV Reflection-Absorption Spectroscopy. *The Journal of Chemical Physics* **2019**, *151* (10), 104701.

(21) Mansourian-Hadavi, N.; Wansom, S.; Perry, N. H.; Nagaraja, A. R.; Mason, T. O.; Ye, L.; Freeman, A. J. Transport and Band Structure Studies of Crystalline ZnRh 2 O 4. *Phys. Rev. B* **2010**, *81* (7), 075112.

(22) Feng, T.; Li, L.; Shi, Q.; Dong, S.; Li, B.; Li, K.; Li, G. Evidence for the Influence of Polaron Delocalization on the Electrical Transport in $LiNi_{0.4+x}$ $Mn_{0.4-x}$ $Co_{0.2}$ O_2. *Phys. Chem. Chem. Phys.* **2020**, *22* (4), 2054–2060.

(23) Verissimo, N. C.; Pires, F. A.; Rodríguez-Gutiérrez, I.; Bettini, J.; Fiuza, T. E. R.; Biffe, C. A.; Montoro, F. E.; Schleder, G. R.; Castro, R. H. R.; Leite, E. R.; Souza, F. L. Dual Modification on Hematite to Minimize Small Polaron Effects and Charge Recombination for Sustainable Solar Water Splitting. *J. Mater. Chem. A* **2024**, *12* (11), 6280–6293.

Chemical Science Accepted Manuscript

View Article Online
DOI: 10.1039/D5SC01909E

Open Access Article. Published on 12 May 2025. Downloaded on 5/16/2025 10:21:16 PM.
This article is licensed under a Creative Commons Attribution 3.0 Unported Licence.

(24) Bandaranayake, S.; Patnaik, A.; Hruska, E.; Zhu, Q.; Das, S.; Baker, L. R. Effect of Surface Electron Trapping and Small Polaron Formation on the Photocatalytic Efficiency of Copper(I) and Copper(II) Oxides. *ACS Appl. Mater. Interfaces* **2024**, *16* (31), 41616–41625.

(25) Gajapathy, H.; Bandaranayake, S.; Hruska, E.; Vadakkayil, A.; Bloom, B. P.; Londo, S.; McClellan, J.; Guo, J.; Russell, D.; De Groot, F. M. F.; Yang, F.; Waldeck, D. H.; Schultze, M.; Baker, L. R. Spin Polarized Electron Dynamics Enhance Water Splitting Efficiency by Yttrium Iron Garnet Photoanodes: A New Platform for Spin Selective Photocatalysis. *Chem. Sci.* **2024**, *15* (9), 3300–3310.

(26) Cheng, C.-S.; Serizawa, M.; Sakata, H.; Hirayama, T. Electrical Conductivity of Co_3O_4 Films Prepared by Chemical Vapour Deposition. *Materials Chemistry and Physics* **1998**, *53* (3), 225–230.

(27) Huang, X. C.; Zhang, J. Y.; Wu, M.; Zhang, S.; Xiao, H. Y.; Han, W. Q.; Lee, T.-L.; Tadich, A.; Qi, D.-C.; Qiao, L.; Chen, L.; Zhang, K. H. L. Electronic Structure and p -Type Conduction Mechanism of Spinel Cobaltite Oxide Thin Films. *Phys. Rev. B* **2019**, *100* (11), 115301.

(28) Carneiro, L. M.; Cushing, S. K.; Liu, C.; Su, Y.; Yang, P.; Alivisatos, A. P.; Leone, S. R. Excitation-Wavelength-Dependent Small Polaron Trapping of Photoexcited Carriers in α-Fe_2O_3. *Nature Mater* **2017**, *16* (8), 819–825.

(29) Shelton, J. L.; Knowles, K. E. Thermally Activated Optical Absorption into Polaronic States in Hematite. *J. Phys. Chem. Lett.* **2021**, *12* (13), 3343–3351.

(30) Shelton, J. L.; Knowles, K. E. Polaronic Optical Transitions in Hematite (α-Fe2O3) Revealed by First-Principles Electron–Phonon Coupling. *The Journal of Chemical Physics* **2022**, *157* (17), 174703.

(31) Freytag, F.; Corradi, G.; Imlau, M. Atomic Insight to Lattice Distortions Caused by Carrier Self-Trapping in Oxide Materials. *Sci Rep* **2016**, *6* (1), 36929.

(32) Yamada, Y.; Hino, O.; Nohdo, S.; Kanao, R.; Inami, T.; Katano, S. Polaron Ordering in Low-Doping La 1 − x Sr x MnO 3. *Phys. Rev. Lett.* **1996**, *77* (5), 904–907.

(33) Allodi, G.; Cestelli Guidi, M.; De Renzi, R.; Caneiro, A.; Pinsard, L. Ultraslow Polaron Dynamics in Low-Doped Manganites from L 139 a NMR-NQR and Muon Spin Rotation. *Phys. Rev. Lett.* **2001**, *87* (12), 127206.

(34) Zhang, S. X.; Kundaliya, D. C.; Yu, W.; Dhar, S.; Young, S. Y.; Salamanca-Riba, L. G.; Ogale, S. B.; Vispute, R. D.; Venkatesan, T. Niobium Doped TiO2: Intrinsic Transparent Metallic Anatase versus Highly Resistive Rutile Phase. *Journal of Applied Physics* **2007**, *102* (1), 013701.

(35) Possenriede, E.; Kröse, H.; Varnhorst, T.; Scharfschwerdt, R.; Schirmer, O. F. Shallow Acceptor and Electron Conduction States in $BaTiO_3$. *Ferroelectrics* **1994**, *151* (1), 199–204.

(36) Cook, J. G.; Van Der Meer, M. P. The Optical Properties of Sputtered Co_3O_4 Films. *Thin Solid Films* **1986**, *144* (2), 165–176.

Chemical Science Accepted Manuscript

View Article Online
DOI: 10.1039/D5SC01909E

Open Access Article. Published on 12 May 2025. Downloaded on 5/16/2025 10:21:16 PM.
This article is licensed under a Creative Commons Attribution 3.0 Unported Licence.

(37) Miedzinska, K. M. E.; Hollebone, B. R.; Cook, J. G. An Assignment of the Optical Absorption Spectrum of Mixed Valence Co_3O_4 Spinel Films. *Journal of Physics and Chemistry of Solids* **1987**, *48* (7), 649–656.

(38) Kim, K. J.; Park, Y. R. Optical Investigation of Charge-Transfer Transitions in Spinel Co_3O_4. *Solid State Communications* **2003**, *127* (1), 25–28.

(39) Qiao, L.; Xiao, H. Y.; Meyer, H. M.; Sun, J. N.; Rouleau, C. M.; Puretzky, A. A.; Geohegan, D. B.; Ivanov, I. N.; Yoon, M.; Weber, W. J.; Biegalski, M. D. Nature of the Band Gap and Origin of the Electro-/Photo-Activity of Co3O4. *J. Mater. Chem. C* **2013**, *1* (31), 4628.

(40) Jiang, C.-M.; Baker, L. R.; Lucas, J. M.; Vura-Weis, J.; Alivisatos, A. P.; Leone, S. R. Characterization of Photo-Induced Charge Transfer and Hot Carrier Relaxation Pathways in Spinel Cobalt Oxide (Co_3O_4). *J. Phys. Chem. C* **2014**, *118* (39), 22774–22784.

(41) Waegele, M. M.; Doan, H. Q.; Cuk, T. Long-Lived Photoexcited Carrier Dynamics of d – d Excitations in Spinel Ordered Co_3O_4. *J. Phys. Chem. C* **2014**, *118* (7), 3426–3432.

(42) Aroonratsameruang, P.; Chakthranont, P.; Pattanasattayavong, P. The Cause of Limited Photoelectrochemical Water Reduction Performance of Co3O4 Photocathodes. *Materials Chemistry and Physics* **2021**, *270*, 124834.

(43) Hayes, D.; Hadt, R. G.; Emery, J. D.; Cordones, A. A.; Martinson, A. B. F.; Shelby, M. L.; Fransted, K. A.; Dahlberg, P. D.; Hong, J.; Zhang, X.; Kong, Q.; Schoenlein, R. W.; Chen, L. X. Electronic and Nuclear Contributions to Time-Resolved Optical and X-Ray Absorption Spectra of Hematite and Insights into Photoelectrochemical Performance. *Energy Environ. Sci.* **2016**, *9* (12), 3754–3769.

(44) Ismail, A. S. M.; Uemura, Y.; Park, S. H.; Kwon, S.; Kim, M.; Elnaggar, H.; Frati, F.; Niwa, Y.; Wadati, H.; Hirata, Y.; Zhang, Y.; Yamagami, K.; Yamamoto, S.; Matsuda, I.; Halisdemir, U.; Koster, G.; Weckhuysen, B. M.; De Groot, F. M. F. Direct Observation of the Electronic States of Photoexcited Hematite with Ultrafast 2p3d X-Ray Absorption Spectroscopy and Resonant Inelastic X-Ray Scattering. *Phys. Chem. Chem. Phys.* **2020**, *22* (5), 2685–2692.

(45) Zhang, Y.; Zhang, C.; Huang, X.; Yang, Z.; Zhang, K. H. L.; Yang, Y. Barrierless Self-Trapping of Photocarriers in Co_3O_4. *J. Phys. Chem. Lett.* **2021**, *12* (50), 12033–12039.

(46) Roth, W. L. The Magnetic Structure of Co_3O_4. *Journal of Physics and Chemistry of Solids* **1964**, *25* (1), 1–10. https://doi.org/10.1016/0022-3697(64)90156-8.

(47) Cococcioni, M.; De Gironcoli, S. Linear Response Approach to the Calculation of the Effective Interaction Parameters in the LDA + U Method. *Phys. Rev. B* **2005**, *71* (3), 035105.

(48) Himmetoglu, B.; Wentzcovitch, R. M.; Cococcioni, M. First-Principles Study of Electronic and Structural Properties of CuO. *Phys. Rev. B* **2011**, *84* (11), 115108.

(49) Zacharias, M.; Patrick, C. E.; Giustino, F. Stochastic Approach to Phonon-Assisted Optical Absorption. *Phys. Rev. Lett.* **2015**, *115* (17), 177401.

(50) Kang, Y.; Peelaers, H.; Krishnaswamy, K.; Van De Walle, C. G. First-Principles Study of Direct and Indirect Optical Absorption in BaSnO3. *Applied Physics Letters* **2018**, *112* (6), 062106.

Chemical Science Accepted Manuscript

View Article Online
DOI: 10.1039/D5SC01909E

(51) Chen, J.; Wu, X.; Selloni, A. Electronic Structure and Bonding Properties of Cobalt Oxide in the Spinel Structure. *Phys. Rev. B* **2011**, *83* (24), 245204.

(52) Singh, V.; Kosa, M.; Majhi, K.; Major, D. T. Putting DFT to the Test: A First-Principles Study of Electronic, Magnetic, and Optical Properties of Co_3O_4. *J. Chem. Theory Comput.* **2015**, *11* (1), 64–72.

(53) Lohaus, C.; Morasch, J.; Brötz, J.; Klein, A.; Jaegermann, W. Investigations on RF-Magnetron Sputtered $Co_3 O_4$ Thin Films Regarding the Solar Energy Conversion Properties. *J. Phys. D: Appl. Phys.* **2016**, *49* (15), 155306.

(54) Lima, A. F. Interpretation of the Optical Absorption Spectrum of Co3O4 with Normal Spinel Structure from First Principles Calculations. *Journal of Physics and Chemistry of Solids* **2014**, *75* (1), 148–152.

(55) Smart, T. J.; Pham, T. A.; Ping, Y.; Ogitsu, T. Optical Absorption Induced by Small Polaron Formation in Transition Metal Oxides: The Case of Co_3O_4. *Phys. Rev. Materials* **2019**, *3* (10), 102401.

(56) Hadjiev, V. G.; Iliev, M. N.; Vergilov, I. V. The Raman Spectra of $Co_3 O_4$. *J. Phys. C: Solid State Phys.* **1988**, *21* (7), L199–L201.

(57) Rivas-Murias, B.; Salgueiriño, V. Thermodynamic CoO–$Co_3 O_4$ Crossover Using Raman Spectroscopy in Magnetic Octahedron-shaped Nanocrystals. *J Raman Spectroscopy* **2017**, *48* (6), 837–841.

(58) White, W. B.; DeAngelis, B. A. Interpretation of the Vibrational Spectra of Spinels. *Spectrochimica Acta Part A: Molecular Spectroscopy* **1967**, *23* (4), 985–995.

(59) Wang, Z.; Nayak, P. K.; Caraveo-Frescas, J. A.; Alshareef, H. N. Recent Developments in P-Type Oxide Semiconductor Materials and Devices. *Adv. Mater.* **2016**, *28* (20), 3831–3892.

(60) Lany, S. Semiconducting Transition Metal Oxides. *J. Phys.: Condens. Matter* **2015**, *27* (28), 283203.

(61) Dekkers, M.; Rijnders, G.; Blank, D. H. A. $ZnIr_2O_4$, a p-Type Transparent Oxide Semiconductor in the Class of Spinel Zinc-D6-Transition Metal Oxide. *Appl. Phys. Lett.* **2007**, *90* (2), 021903.

(62) Venkatachalam, V.; Alsalme, A.; Alswieleh, A.; Jayavel, R. Double Hydroxide Mediated Synthesis of Nanostructured $ZnCo_2O_4$ as High Performance Electrode Material for Supercapacitor Applications. *Chemical Engineering Journal* **2017**, *321*, 474–483.

(63) Wang, W. Facile Hydrothermal Synthesis of ZnCo2O4 Nanostructures: Controlled Morphology and Magnetic Properties. *J Mater Sci: Mater Electron* **2021**, *32* (12), 16662–16668.

(64) Ž. Lazarević, Z.; Jovalekić, Č.; Milutinović, A.; Sekulić, D.; Ivanovski, V. N.; Rečnik, A.; Cekić, B.; Ž. Romčević, N. Nanodimensional Spinel $NiFe_2O_4$ and $ZnFe_2O_4$ Ferrites Prepared by Soft Mechanochemical Synthesis. *Journal of Applied Physics* **2013**, *113* (18), 187221.

Open Access Article. Published on 12 May 2025. Downloaded on 5/16/2025 10:21:16 PM.
This article is licensed under a Creative Commons Attribution 3.0 Unported Licence.

Chemical Science Accepted Manuscript

View Article Online
DOI: 10.1039/D5SC01909E

Open Access Article. Published on 12 May 2025. Downloaded on 5/16/2025 10:21:16 PM.
This article is licensed under a Creative Commons Attribution 3.0 Unported Licence.

Chemical Science Accepted Manuscript

View Article Online
DOI: 10.1039/D5SC01909E

Data supporting this article have been included as part of the ESI. Primary data are available from the authors upon reasonable request.

Open Access Article. Published on 12 May 2025. Downloaded on 5/16/2025 10:21:16 PM.
This article is licensed under a Creative Commons Attribution 3.0 Unported Licence.

Chemical Science Accepted Manuscript